



Optimization of process parameters for the development of Ni–Al–Ti–Mn–Co–Fe–Cr high entropy alloy system via spark plasma sintering

Emmanuel Olorundaisi¹ · Bukola Joseph Babalola¹ · Bamidele Lawrence Bayode¹ · Linda Teffo² · Peter A. Olubambi¹

Received: 6 February 2023 / Accepted: 21 March 2023 / Published online: 31 March 2023
© The Author(s) 2023

Abstract

A novel equal atomic Ni–Al–Ti–Mn–Co–Fe–Cr high entropy alloy (HEA) was developed via the spark plasma sintering (SPS) process. This study investigates the influence of the sintering parametric processes, which consist of the sintering temperature (ST) and heating rate (HR) at constant pressure and dwelling time (DT) on the Microhardness (MH) and relative density (RD) of the developed HEA. Response surface methodology (RSM) was used to develop a predictive model. The design of experiment (DOE) approach was adopted to reduce the number of experiments and eliminate trial by error. ST and HR were considered model variables in developing the model. The user-defined design (UDD) under RSM was used to predict the optimal sintering parameters, and an experiment was conducted to validate the result. The result indicates that ST and HR play a significant role in achieving high densification and hardness. The developed alloy shows the highest MH value of 136.3 HV at 850 °C and an HR of 100 °C/min. Equally, the least crystallite size of 2.05 µm was realized at the maximum ST. However, the modeling response suggested that full densification of about 99% can be achieved at an ST of 850 °C, a pressure of 50 MPa, a DT of 5 min, and an HR of 100 °C/min.

Keywords High entropy alloy · Phase formation · Crystal structure · Response surface methodology · Microhardness · Relative density

1 Introduction

The actualization of the 4.0 industrial revolution has become a global phenomenon because of its role in reducing carbon emissions. Hence, the quest for a high-strength to lightweight material with excellent corrosion, wear, and creep resistance is increasing. The aviation, automobile, marine, and chemical processing industries demand fully dense, high-strength, tough materials for high-temperature applications and lightweight materials that can withstand stress. Metallic

alloys such as aluminium, titanium, and nickel-based superalloys have been employed to meet this requirement [1, 2]. However, these alloys are characterized by high-density characteristics requiring a high mechanical load to operate. This consequently results in increased fuel consumption and carbon emission to the environment. The emergence of NiAl is a potential candidate material with the capabilities to replace these alloys. It possesses high-temperature capability to the tune of 1638 °C. The thermal and mechanical stability at elevated temperatures and low-density characteristics are added advantages. Nickel aluminide has gained attraction in developing lower-weight to high-strength structural alloys with an advantage of strengthening the second phase for extreme temperature applications. Nickel and aluminium have a strong bond at extreme temperatures. This bond has generated outstanding properties at an extreme temperature and good strength that could effectively compete with superalloys and ceramics. The NiAl-based alloy has shown superior thermomechanical properties, excellent corrosion, wear, and creep resistance compared to the conventional

✉ Emmanuel Olorundaisi
olorundaisiemmanuel@gmail.com

¹ Centre for Nanoengineering and Tribocorrosion, School of Mining, Metallurgy and Chemical Engineering, University of Johannesburg, Johannesburg 2092, South Africa

² Institute for Nanoengineering Research, Department of Chemical, Metallurgical and Materials Engineering, Tshwane University of Technology, Pretoria, South Africa

nickel-based superalloys [1–6]. Nickel-aluminide is an intermetallic compound containing aluminium and nickel and has been the focus of recent researchers. The two most widely known are Ni_3Al and NiAl . However, for this study, we will focus on fabricating Ni–Al–Ti–Mn–Co–Fe–Cr HEA.

The intermetallic compounds are composed of two or more elemental metals in different ratios, forming new properties and crystal structures different from their constituents' elements, such as nickel aluminides. These intermetallic materials are alloyed to obtain more desirable properties. Most importantly, the nickel aluminides; γ' (Ni_3Al : $L1_2$) and β' (NiAl : B2) are known for their strength and brittleness with excellent mechanical properties at an elevated temperature [7–9]. They also often exhibit excellent magnetic, superconducting, and chemical properties because of strong internal order and mixed (metallic and covalent/ionic) bonding [10]. As a result, they have found applications in hydrogen storage materials, turbine blades, barrier and contact layers in microelectronics, automobile industries, aerospace, etc. Due to its wide range of acceptance, a lot of research has gone into improving its mechanical properties through microalloying and production processes. [11, 12]. Hence, adopting a new approach to optimize NiAl alloy by alloying with other elements is imperative. Therefore, incorporating highly stable metals in the nanoscale rendered a super strength to NiAl alloy both at room and higher temperatures, improving the hardness and enhancing creep and corrosion resistance.

Further to the actualization of the industrial 4.0 revolution came high entropy alloys (HEA). The HEA adopted the idea of mixing different primary elements in an equal or near-equimolar ratio to produce a multi-component alloy rather than the conventional alloying of a single-based element or compound to form the matrix. The deviation from the conventional single alloying system has left a design gap to be explored to meet the industrial revolution. Given this, this research was birthed to develop Ni–Al–Ti–Mn–Co–Fe–Cr HEA. High entropy alloy is a new class of alloys with excellent mechanical properties at elevated temperatures [13]. In the past 16 years, HAE has drawn significant research because of its unique properties and by defying the principles of alloying in existence for many years. It has been established that HEA is suitable for use due to its numerous properties, ranging from high strength to thermostability and corrosion resistance, thus increasing its developmental potential [14]. In the space of 16 years, HEA has attracted so much interest from different fields. Studies have been carried out on its physical properties, such as magnetic, electrical, or thermal, by Tsai [15] and Zhang et al. [16]. Researchers have investigated the corrosive behavior and HEA's excellent mechanical performance and deformation behavior. This has expanded its application at elevated and cryogenic temperatures [17–25]. Figure 1 describes HEA

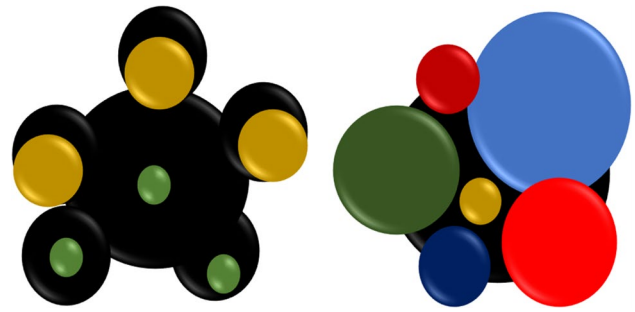


Fig. 1 Schematic diagram of high entropy alloy composition in at. %

with different circle sizes representing the ratio in at.% of the alloying elements in the final alloy.

The development of Ni–Al–Ti–Mn–Co–Fe–Cr HEA will be a groundbreaking achievement in solving most of the challenges associated with NiAl. There is so much prospect in NiAl if the limitations can be addressed. To develop Ni–Al–Ti–Mn–Co–Fe–Cr HEA, careful consideration must be given to the characteristics of the continuous matrix material, the type or nature of constituent elements, the percentage weight composition of the alloys in the matrix, the particle size, the binding nature of the continuous-discontinuous material interface, and the processing technique employed to modify the microstructural evolution [26].

Process and material selection are essential factors in developing Ni–Al–Ti–Mn–Co–Fe–Cr HEA. The mechanical alloy method will produce fully pre-alloyed Ni–Al–Ti–Mn–Co–Fe–Cr HEA powders, and spark plasma sintering (SPS) will provide the ideal consolidation method. Indisputably, the SPS process has been demonstrated to be excellent powder metallurgy (PM) approach to developing nanostructured ultrafine-grained materials due to their flexibility in fabricating complex shapes. It produces highly dense consolidated solid materials with good bonding structure and barrier to the coarsening of grains [27]. This process enhanced the consolidation of solid bulk materials at a low temperature. It enabled the addition of a larger percentage of particles that are traditionally impossible to fabricate by other processing methods.

In this present research, NiAl alloyed with titanium (Ti), manganese (Mn), iron (Fe), cobalt (Co), and chromium (Cr) was fabricated using the spark plasma sintering process of powder metallurgy. The effect of these alloying elements cannot be over-emphasized. These alloying elements are employed to improve the mechanical properties of HEA developed [28, 29]. When alloying, it is worth noting that the alloying elements influence the final properties of the developed HEA, such as the melting point, density, and lattice constant. Therefore, the fabrication of a novel HEA Ni-14.29Al-14.29Ti-14.29Mn-14.29Co-14.29Fe-14.29Cr-14.29 (at.%) using the spark plasma sintering route to study the

influence of sintering parameters (sintering temperature (ST), and the heating rate (HR)) on the relative density (RD), and microhardness (MH) is the focus of this study. The user-defined design of response surface methodology (UDD-RSM) was applied to optimize the process parameters (ST and HR) to improve the mechanical properties of Ni-14.29Al-14.29Ti-14.29Mn-14.29Co-14.29Fe-14.29Cr-14.29 (at.%). RSM is a statistical technique that uses experimental designs to develop mathematical models with linear, quadratic, or interaction terms for optimum performance from given factors and response variables [30, 31]. Adopting this technique reduces the number of experimental trials required to evaluate multiple parameters and their interaction. It is essential to state that the outcome of the properties is a function of the combined factorial effect of sintering parameters.

2 Materials and methods

2.1 Thermodynamic simulation

Thermodynamic simulations were performed using THERMOCALC software version 2021b with the TCHEA5 HEAs database. This was employed to determine the amount of phases and phases formed, the solidus and liquidus temperature of the developed HEAs. The alloy’s applicable solidus and liquidus temperatures were understood and used as a guide for the sintering of the alloy.

2.2 Experimental materials

Thermo Fisher Scientific supplied the powders used in this research, with details shown in Table 1.

2.3 Design of experiment

Design of experiment (DOE) became widely accepted due to the possibilities of minimizing the number of experimental runs and trial by error, reducing production cost. The DOE was first introduced in the 1920s by R.A Fisher for statistical

Table 1 Details of starting powders

Elements	% Purity	Particle size (μm)
Al	99.8	<25
Ni	99.8	<25
Ti	99.6	<25
Mn	99.6	<10
Co	99.5	<37
Fe	99.6	<15
Cr	99.2	<10

modeling and to determine the effects of individual parameters and interactions between parameters on any design output [32]. This method employed both mathematical and statistical techniques. This was done using UDD-RSM to optimize the parameters required to enhance the mechanical properties of the developed HEA. However, this technique has been proven to be reliable by different researchers [30, 31, 33, 34]. Tables 2 and 3 show the model’s buildup information and the factors’ coded and actual operating conditions, respectively. In this research, ST and HR were the controlled parameters. Using Design Expert 13 software, two factors-three levels UDD was applied, and a total of 9 experimental runs were obtained, with a 95% confidence interval (Table 4). The experimental and statistical data were analyzed using analysis of variance (ANOVA). Since the number of levels is just three, the appropriate model to adopt was the second-order polynomial model given in Eq. (1) [35, 36].

$$Y = \beta_0 + \sum_{j=1}^k \beta_j X_j + \sum_{j=1}^k \beta_{jj} X_j^2 + \sum_i \sum_{<j=2}^k \beta_{ij} X_i X_j + e_i \tag{1}$$

where

- Y is the predicted response
- k is the number of studied factors
- X_i and X_j are the variables (factors)
- β₀ is the constant coefficient
- β_j, β_{jj}, β_{ij} are the interaction coefficients of linear, quadratic, and second-order terms. e_i is the error

2.4 The procedure of the spark plasma sintering process

The powders were measured based on the designed weight composition (Table 5) and placed in an air-tight container for subsequent homogenous alloy mixing using a tubular mixer

Table 2 Buildup information for RSM model

File version	Design Expert 13.0.5.0	Build time (ms)	2.00
Study type	Response surface	Subtype	Randomized
Design type	User-defined	Runs	9
Design model	Quadratic	Blocks	No blocks

Table 3 Coded and actual operating conditions of the factors

Factor	Name	Units	Type	Minimum	Maximum	Coded low	Coded high	Mean	Std. Dev
A	ST	°C	Numeric	750	850	-1 ↔ 750.00	+1 ↔ 850.00	800	43.30
B	HR	°C/min	Numeric	80	100	-1 ↔ 80.00	+1 ↔ 100.00	90	8.66

Table 4 Design of experiments (DOE)

Run	Sample	Factor 1 A: ST (°C)	Factor 2 B: HR (°C/min)
1	h	850	90
2	d	800	80
3	e	800	90
4	f	800	100
5	a	750	80
6	c	750	100
7	g	850	80
8	b	750	90
9	i	850	100

at 150 rpm for 12 h. A spark plasma sintering machine, model SPS FCT Systeme GmbH, Germany, was utilized to consolidate the mixed powders of Ni–Al–Ti–Mn–Co–Fe–Cr in equal atomic percent. The measured admixed metal alloys were poured into a 20 mm graphite die with the right punches. A graphite sheet was used to create space between the powder and the inner wall of the graphite die before the powder was added. This was done to make it easier to remove the consolidated powder after sintering and to lessen the temperature difference on the workpiece. The samples were sintered according to the design in Table 4 at a constant pressure of 50 MPa and dwelling time of 5 min. Afterward, the sintered samples were taken out of the graphite die, sandblasted to eliminate the impurities, and exposed to metallographic treatment by grinding and polishing.

2.5 Characterization and analysis of the sintered samples

2.5.1 Density analysis

The density of the sintered alloys was determined using a densitometer, which functions based on Archimedes principles. The measurement was carried out five times, and the mean value was reported as the mean experimental density. The theoretical density was also determined using the mixture's

rule as expressed in Eq. (2). Using Eqs. (3) and (4), the alloys' relative density and percentage porosity obtained from the experimental density were assessed.

$$\text{Theoretical density} = \left(\frac{\%Ni}{\rho Ni} + \frac{\%Al}{\rho Al} + \frac{\%Ti}{\rho Ti} + \frac{\%Mn}{\rho Mn} + \frac{\%Fe}{\rho Fe} + \frac{\%Mn}{\rho Mn} + \frac{\%Cr}{\rho Cr} \right)^{-1} \quad (2)$$

$$\text{Relative density} = \left(\frac{\text{Experimental density}}{\text{Theoretical density}} \times 100 \right) \% \quad (3)$$

$$\text{Percentage Porosity} = 100\% - \text{Relative density} \quad (4)$$

2.5.2 Microstructure and crystalline phase characterization

After being hot mounted with a Struers CitoPress-1 Machine, the prepared samples were ground and polished with a Struers TegraPol-11 550 Machine, utilizing successive disc grades of 90, 220, and 330. The samples were then washed and air-dried, followed by etching with a Keller's etchant (190 ml distilled water, 5 ml nitric acid, 3 ml hydrochloric acid, and 2 ml of hydrofluoric acid). After this, a scanning electron microscope model JEOL JSM-7900F was used to observe how the sintered sample's microstructure had changed. The microscope revealed each designed sample's grain boundaries (neck formation). Additionally, the crystalline phase and chemical present in the samples were investigated using X-ray diffraction (XRD) at a wavelength of 1.5406 and K-alpha of 0.94. The Scherrer formula, as expressed in Eq. (5), was used to determine the size of the crystallites present in each sample at the nanoscale.

$$D = \frac{K\lambda}{\beta \cos\theta} \quad (5)$$

where

D is the crystallites size

K is the Scherrer constant given as 0.9

λ is the wavelength of the X-ray used given as 0.154060 μm

Table 5 Compositions of the elements of the alloys

Elements	Al	Ni	Ti	Mn	Co	Fe	Cr
Sample in at. %	14.286	14.286	14.286	14.286	14.286	14.286	14.286
Sample in wt. %	7.59	16.52	13.48	15.47	16.59	15.72	14.64

β is the FWHM (Full width at half of the maximum) in radians

θ is the peak position in radians

2.5.3 Microhardness

Using a diamond indenter-equipped Vickers tester, model FM-800, the micro-hardness was assessed. This was done with an applied load of 100 gf for 15 s dwell time at 0.5 mm spacing. Five indentations were taken for each sintered sample, and the effective mean hardness was calculated and recorded.

3 Results and discussion

3.1 Microstructural study of the sintered samples

Figure 2 shows the SEM image of the admixed powders. The constituent elements in the admixed powder exhibited a highly homogenous state, as shown in Fig. 3. The SEM and EDS analysis reveals the powder's morphology and ascertains the chemical constituent.

However, Fig. 4 represents the microstructure obtained under different sintering conditions, as shown in Table 4, at a constant pressure of 50 MPa and dwelling time of 5 min. As the ST increases, the necking between particles increases, which initiates stronger inter-particle bonding and reduction of pores while the porosity reduces. The bonding between the particles increases as the ST increases, thereby improving the packing density of the powder. It could also be observed that as the ST increases, the microstructural refinement increases. The reduction in pore space and higher densification observed could be attributed to condensation and diffusion of constituent elements during the sintering process at the given ST [27]. Figure 4g, h, and i shows fully formed adhesion of particles and excellent microstructural

refinement. Hence, it could be stated that to achieve excellent densification and strong material bonding, it is imperative to sinter at a high ST and HR. These parameters improve particle wettability and diffusion at grain boundaries, which in turn improve the bonding structure and properties of the developed HEA.

3.2 Phase analysis

The amount of phase formed and the identification of the different phases achieved by the alloys were predicted via CALPHAD-based tools using ThermoCalc software. Figures 5 and 6 show the amount of phase and phase diagram, respectively. The master alloy shows only the presence of the BCC phase as seen from the XRD result in Fig. 7. This phase is responsible for the high brittleness of NiAl [11]. Alloying of this master alloy introduced an additional phase (FCC and sigma). This result is further established experimentally with the XRD result in Fig. 7.

The XRD pattern was analyzed to examine the phase composition. The strong bonding among the alloys results from the wettability between the NiAl and the 13.48 wt.%Ti-15.47 wt.%Mn-16.59 wt.%Co-15.72 wt.%Fe-14.64 wt.%Cr. The XRD result coincides with that of the THERMOCALC. Three dominant phases were identified (BCC, FCC, and SIGMA). The lattice parameters and the miller indices (1 1 1 and 1 1 2) indicate that the crystal structure is body-centered cubic (BCC) and face-centered cubic (FCC) [37–43]. It would be noticed that as the ST increases, the peak also increases. Another interesting observation is the crystallite size, as seen in Table 6, which decreases with increasing temperature. The chemical composition and thermal histories of the developed HEA affect the degree of crystallization [38, 41, 43]. The physical and mechanical properties of the developed HEA are influenced mainly by its size; these properties improve as size decreases. [37]. These phases are responsible for the changes observed in the refinement of the grain structure.

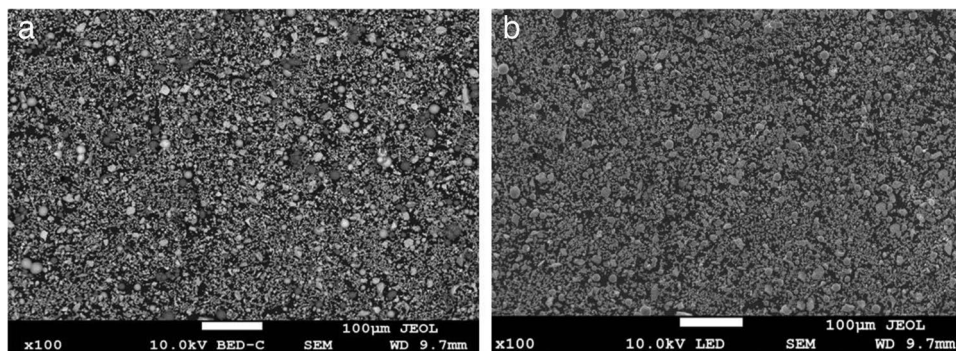


Fig. 2 SEM of mixed $\text{Ni}_{14.29}\text{Al}_{14.29}\text{Ti}_{14.29}\text{Mn}_{14.29}\text{Co}_{14.29}\text{Fe}_{14.29}\text{Cr}_{14.29}$

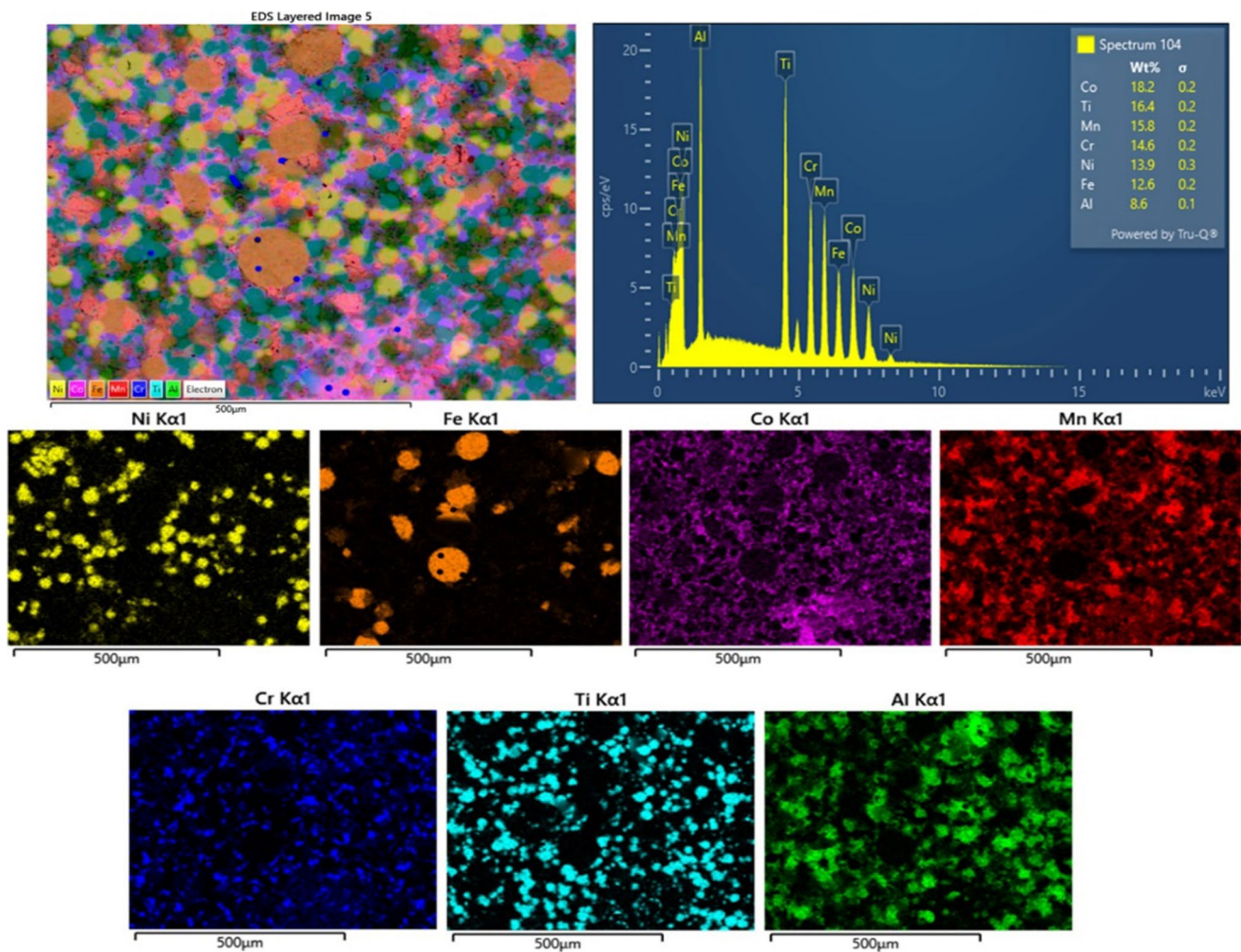


Fig. 3 EDS analysis of sintered $\text{Ni}_{14.29}\text{Al}_{14.29}\text{Ti}_{14.29}\text{Mn}_{14.29}\text{Co}_{14.29}\text{Fe}_{14.29}\text{Cr}_{14.29}$

3.3 Mechanical analysis

Table 7 presents the mechanical properties of the developed HEA. It is evident that the MH increases with a corresponding increase in ST. These increases were justifiable given the crystalline size outcome. Also, from the SEM result in Fig. 3, the volume fraction of pores could be seen to reduce as the ST and HR increase, which is directly proportional to the hardenability of the material [44–47]. Figure 8 shows the MH variation. It was observed that as the ST increases, the hardness also increases. It was also observed that as the ST increases, the density also increases. This implies that as the ST increases, the diffusion rate is enhanced; hence, pores are rapidly closed, leading to porosity reduction and microstructure refinement [44–47]. Therefore, as the ST and HR increase, there is a corresponding increase in weight and improvement in strength [27].

3.4 Model adequacy checking

The model's accuracy is a crucial component of this research because it is essential for ensuring that the model fits and offers a good approximation of the real system. Figure 9 displays the normal probability plot of the studentized residuals for MH and RD to demonstrate the model's suitability. Inferring that the data is normally distributed, it was seen from the result that the points follow a straight line [48].

3.5 Interaction of variables

To ensure the model's fitting, the interaction between the variables (ST and RD) employed to enhance the mechanical properties of the developed HEA was verified. The perturbation plot in Fig. 10 describes the effect of all the factors at optimal when all the experimental conditions in the design space are compared. The response is more

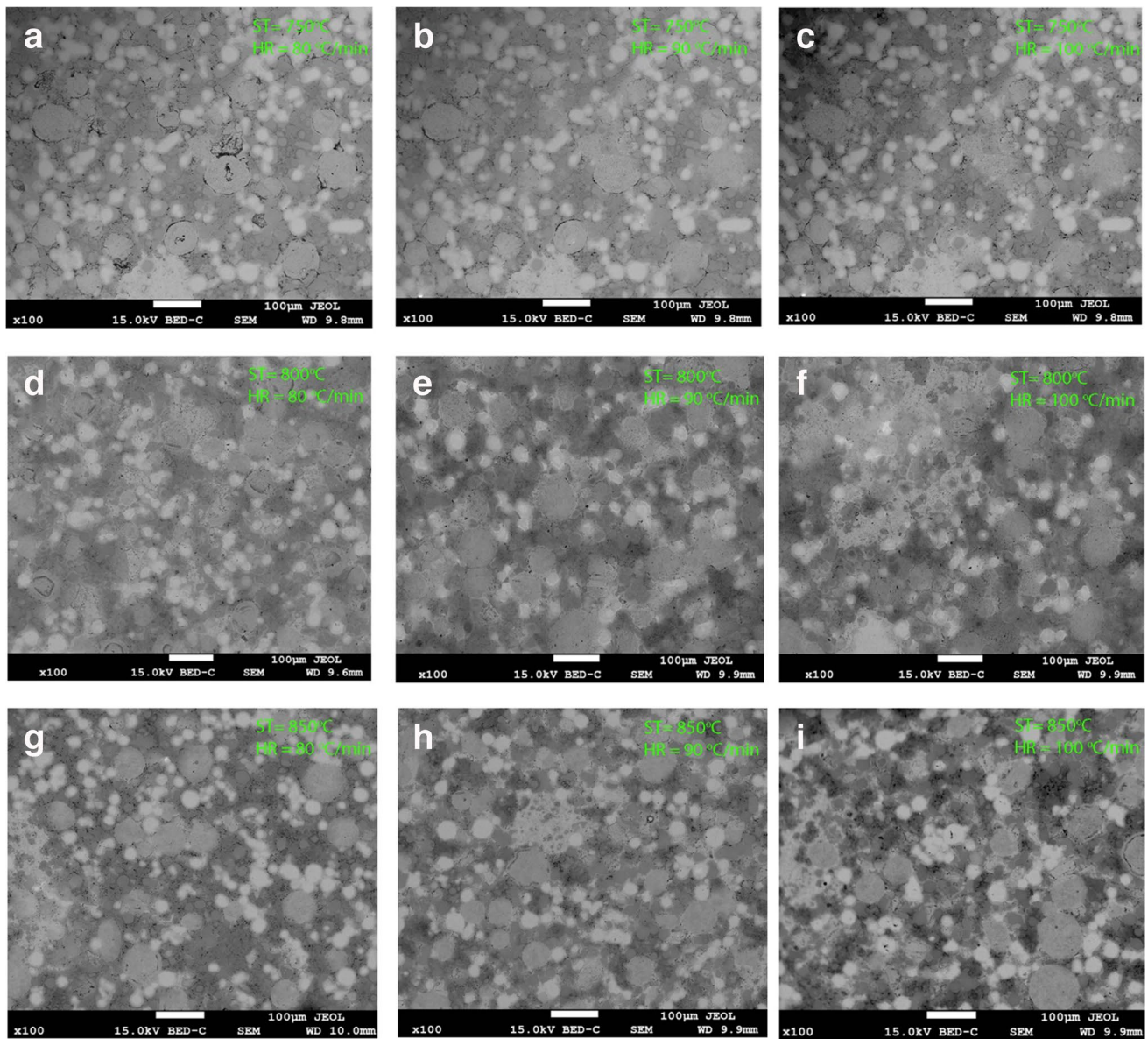


Fig. 4 SEM of sintered $\text{Ni}_{14.29}\text{Al}_{14.29}\text{Ti}_{14.29}\text{Mn}_{14.29}\text{Co}_{14.29}\text{Fe}_{14.29}\text{Cr}_{14.29}$ at varying sintering processing parameters

affected by the factor with a sharper curvature [30, 49]. When the impacts of all the factors were compared, it was found that MH and RD were more sensitive to ST than HR. ST is represented by the coded value A, and HR by the coded value B.

The residual versus run plots in Fig. 11 show if the design points are within the control limit. The red lines indicate the control limits from 4.6553 to -4.6553 for both MH and RD. The design points must lie between the control limits for the model to be valid. Figure 11 established the model's validity, as it was clearly observed that the design points fall between the control limits.

Figure 12 shows the contour plot for the interactive effects of ST and HR on the MH and RD at a design point above

the predicted value. The contour pattern describes the relationship between the factors [50, 51]. The surface response graph shows the optimal process parameters that produce the response's maximum or minimum value [52]. In this work, the optimum MH was observed as the ST and HR increased.

3.6 Development of a regression model equation

The design matrix of the nine experimental runs alongside the coded factors for each variable was employed in determining all the constants in Eq. (1). The software used a quadratic model for the MH and RD for the responses. The parameters were coded with three coding levels for each variable, as shown in Table 4. Table 5 data were regressed

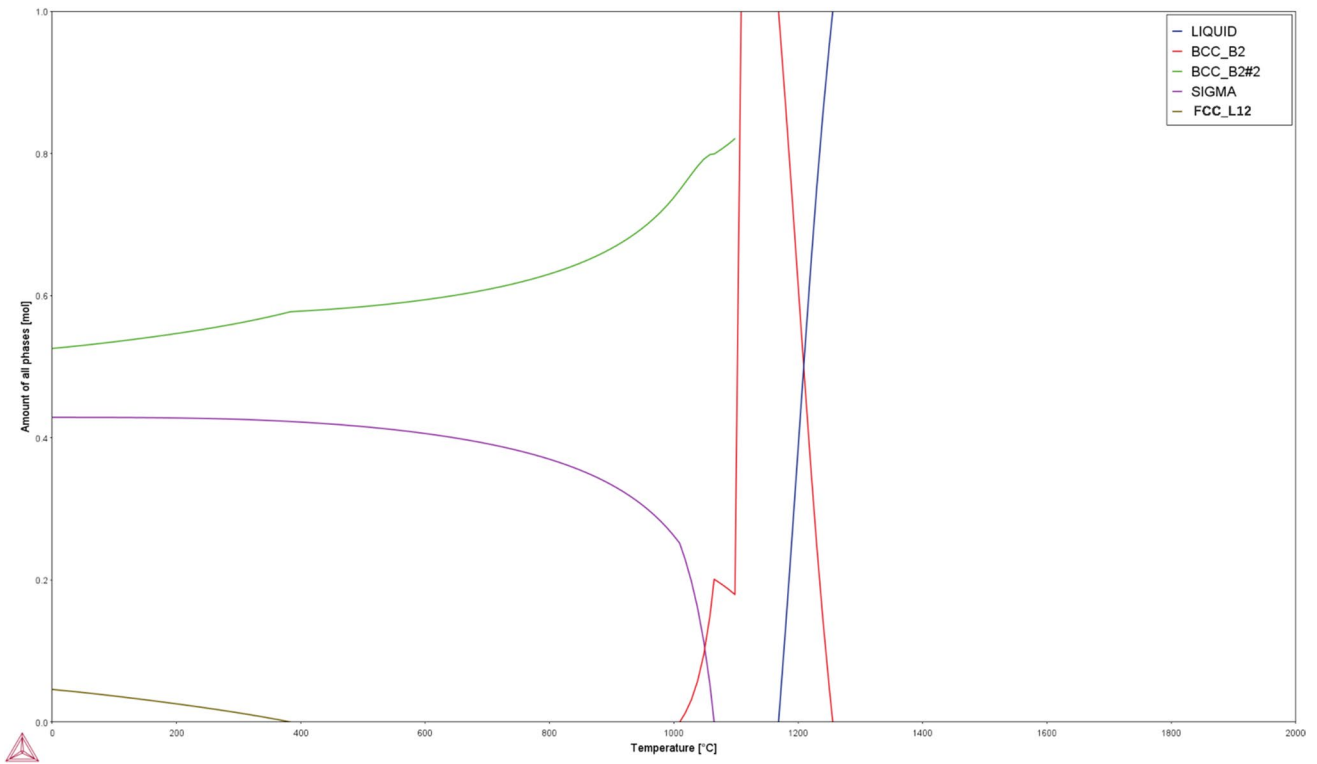
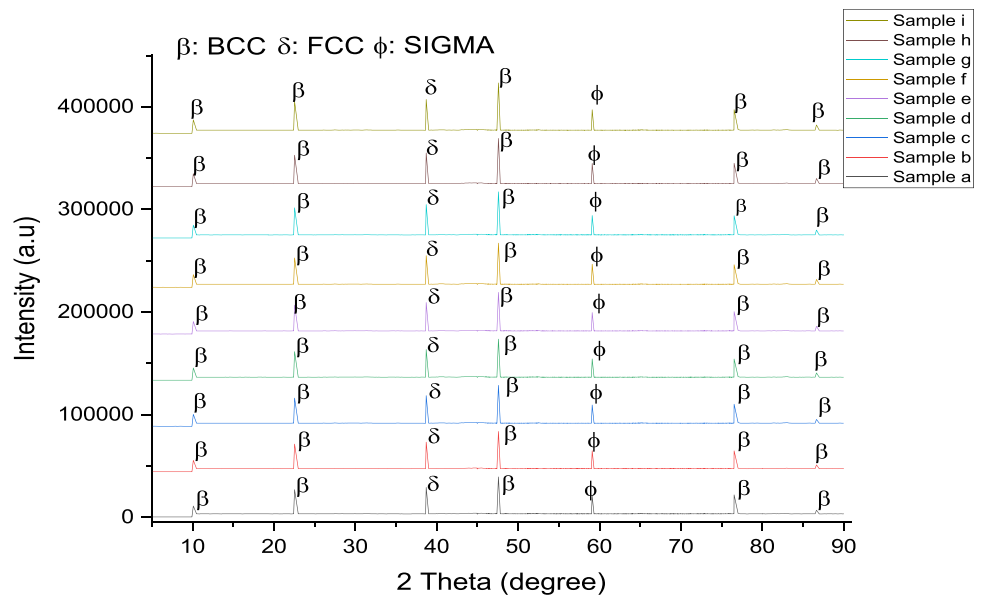


Fig. 5 $\text{Ni}_{14.29}\text{Al}_{14.29}\text{Ti}_{14.29}\text{Mn}_{14.29}\text{Co}_{14.29}\text{Fe}_{14.29}\text{Cr}_{14.29}$ amount of phase

Fig. 6 The XRD phases of the sintered samples



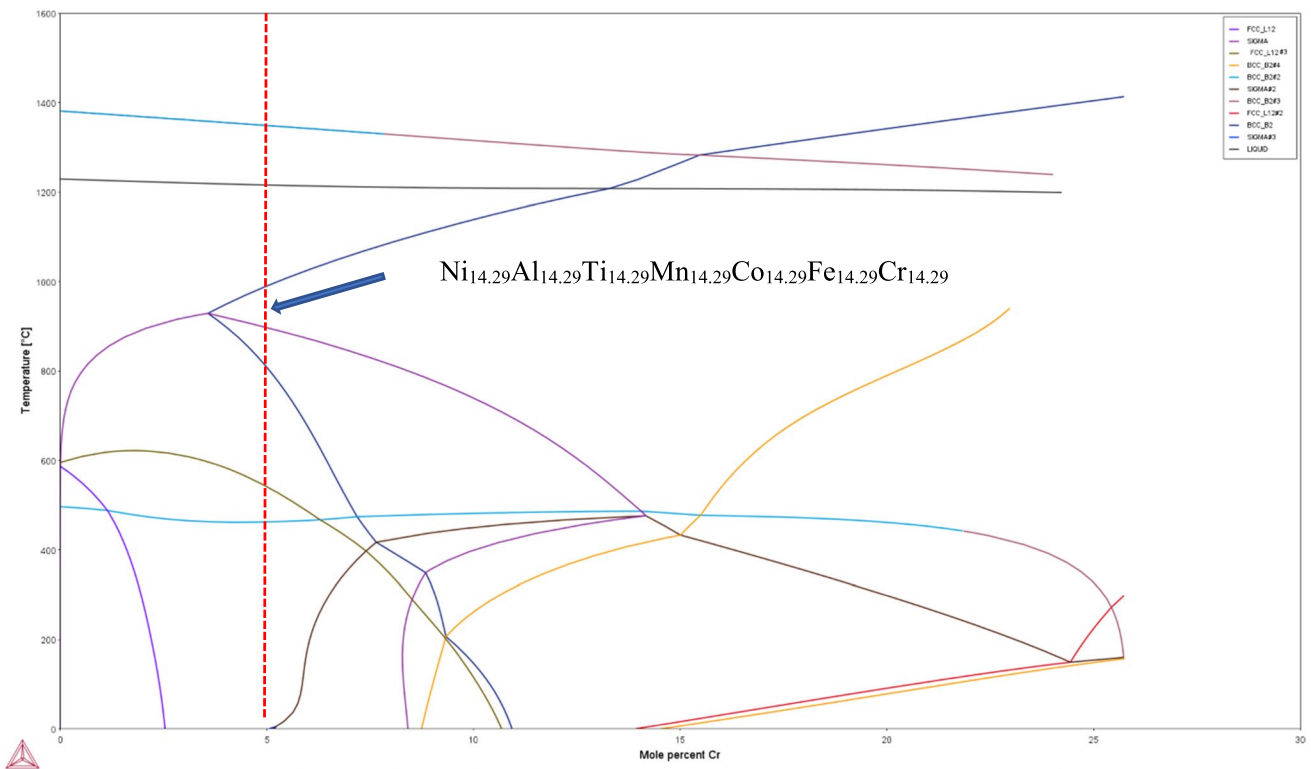


Fig. 7 Ni_{14.29}Al_{14.29}Ti_{14.29}Mn_{14.29}Co_{14.29}Fe_{14.29}Cr_{14.29} phase diagram

Table 6 The crystallite size of the Equal atomic nano-Ni–Al–Ti–Mn–Co–Fe–Cr HEA at different optimized conditions

Sample	Crystallite size (μm)
a	3.81
b	3.15
c	2.71
d	2.53
e	2.47
f	2.37
g	2.18
h	2.17
i	2.05

$$RD = +97.96 + 1.25A + 0.3016B \tag{8}$$

$$RD = +75.23096 + 0.025021ST + 0.030162HR \tag{9}$$

where

A represents the coded value for Sintering Temperature

B represents the coded value for Heating Rate

ST represents Sintering Temperature, HR represents the Holding Time

MH represents the Microhardness Hardness

RD represents the Relative Density

by Design Expert 13.05.0 to develop a mathematical model for the coded and actual values. A second-order polynomial was used to correlate the response and variable values for MH and RD. The final equations in terms of coded and actual factors are represented in Eqs. (6–9).

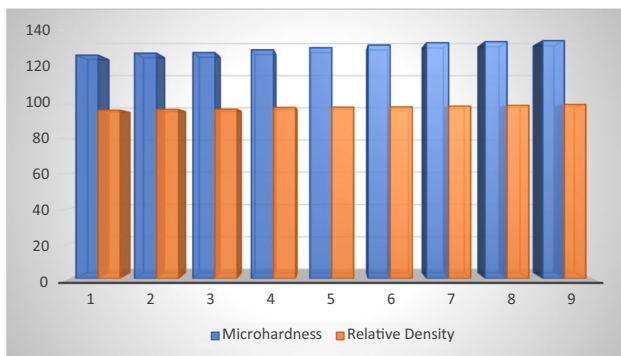
$$MH = +132.34 + 3.40A + 0.8967B \tag{6}$$

$$MH = +69.91889 + 0.067933ST + 0.089667HR \tag{7}$$

The positive sign in the equations indicates synergy effects. This sign also implies that the response improved with an increase in the factor level [49]. The coefficients with one factor of ST and HR represent the effect of that factor. For a specific level of each factor, the equations can predict the response. By default, the high levels of the factors are coded as + 1, and the low levels are coded as – 1 in the equation in terms of coded factors. However, for the actual factor, the levels must be provided in the original

Table 7 Design of experiments, response, and prediction table

Sample	Factor 1 A: T (°C)	Factor 2 B: HR (°C/min)	Response 1 MH (HV)	Response 2 RD	Prediction 1 MH (HV)	Prediction 2 RD
a	750	80	128.02	96.309	128.04	96.41
b	750	90	129.2	96.7468	128.94	96.71
c	750	100	129.5	96.8936	129.84	97.01
d	800	80	131.1	97.9339	131.44	97.66
e	800	90	132.3	98.0843	132.34	97.96
f	800	100	133.8	98.2352	133.23	98.26
g	850	80	135.1	98.6907	134.84	98.91
h	850	90	135.7	99.1504	135.73	99.21
i	850	100	136.3	99.6145	136.63	99.51

**Fig. 8** Variation in MH and RD of the developed HEA

units for each factor [30]. By comparing the factor coefficients, the coded equation aids in determining the relative importance of the factors. The actual equation, however,

cannot be used because the coefficients have been scaled to account for each factor's units, and the intercept is not located in the middle of the design space [30].

3.7 Model validation

The resulting standard deviation, R^2 , and Adjusted R^2 values are used to verify the proposed model's accuracy. The model is accurate if the Adeq Precision score is greater than four and the discrepancy between the Predicted R^2 and Adjusted R^2 is less than 0.2 [31, 53]. While the value of Adeq Precision represents the signal-to-noise ratio, the value of R^2 shows the significance and acceptability of the developed model. The model is valid and can be used to examine the design space, according to the result in Table 8.

Figure 13 shows the relationship between the actual and the predicted response. The plots all follow a similar pattern; this implies that the experimental data and the model agree.

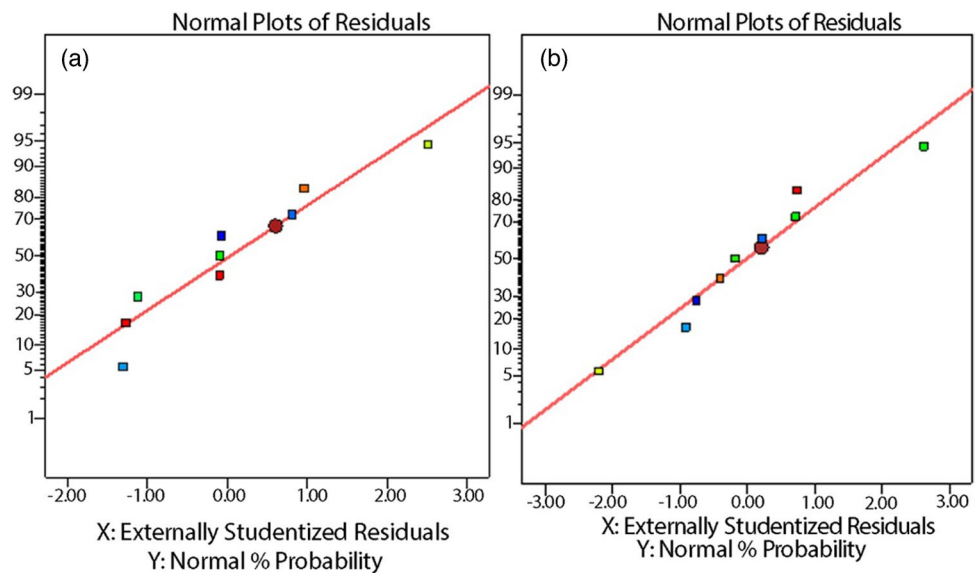
Fig. 9 Normal probability plot for (a) MH and (b) RD

Fig. 10 Perturbation plot for (a) MH, and (b) RD

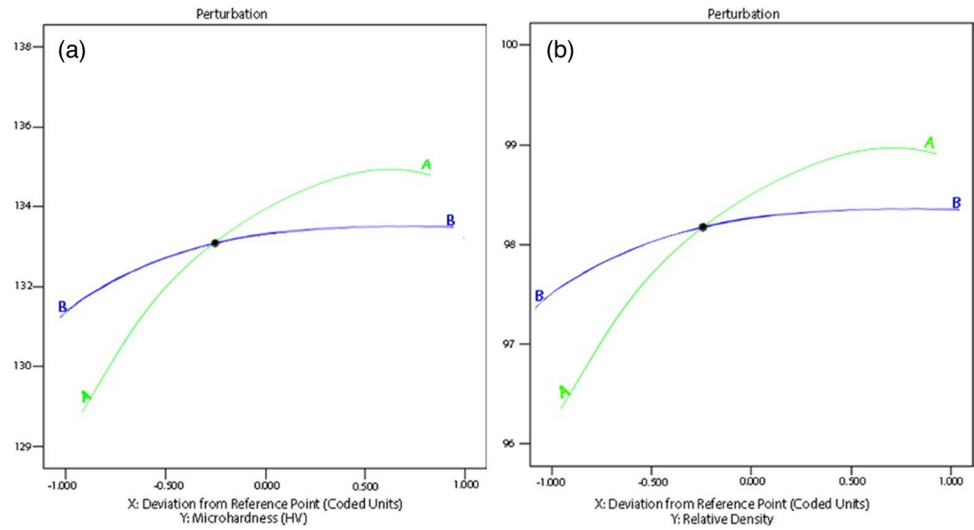


Fig. 11 Residual plot for (a) MH and (b) RD

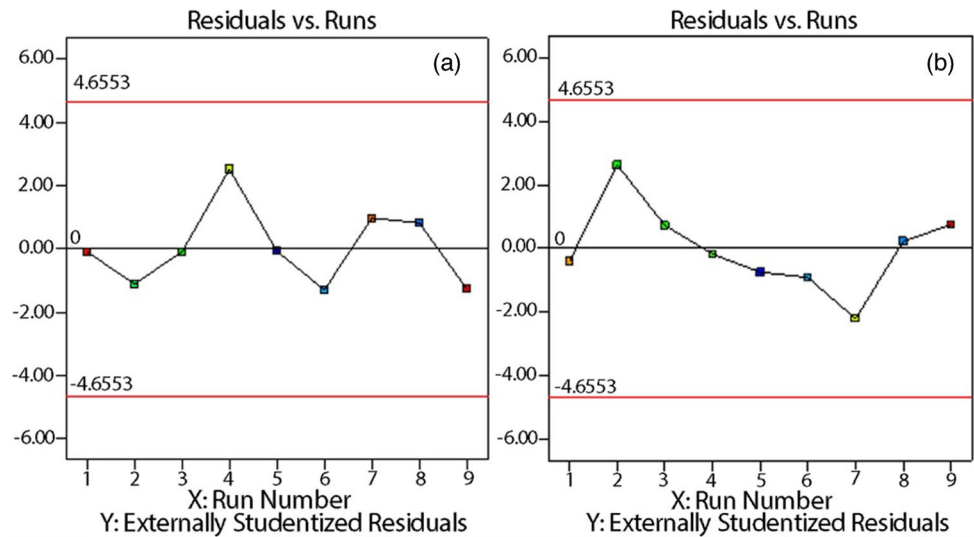


Fig. 12 Contour plot of interaction between HR and ST on (a) MH and (b) RD

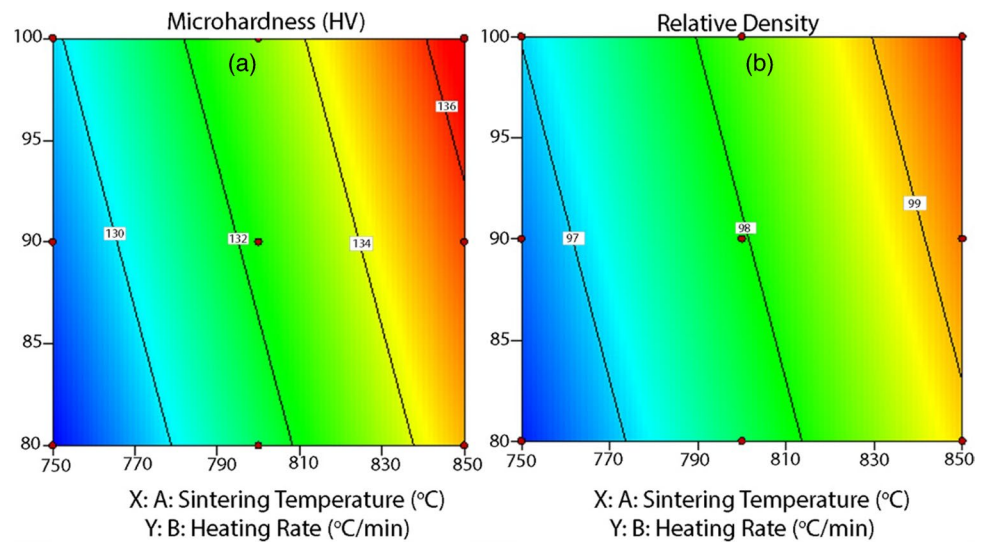
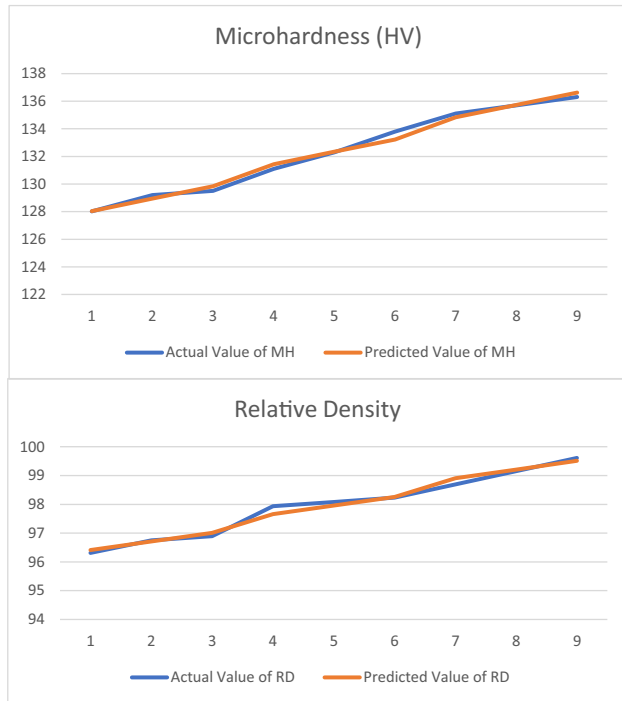


Table 8 Model validation for SH

Test	Predicted R^2	Adjusted R^2	Difference	Adeq. precision
MH	0.9744	0.9858	0.0114	40.758
RD	0.9563	0.9764	0.0201	31.169

**Fig. 13** Comparison of experimental and predicted results for MH and RD

3.8 ANOVA and statistical significance of the model

ANOVA was employed to validate the validity and importance of the model. The model term is significant if the

resulting P -values are less than 0.1. In this study, MH and RD shows P -values of less than 0.0500; hence, the coded A and B for MH and RD are significant model terms. The Model F -value for MH and RD is 278.07 and 166.84, respectively, which implies that the model is also significant. The possibility that the obtained F -values result from noise is extremely low (0.01%). Table 9 shows the statistical analysis of the model, where the factor coding is coded, and the sum of squares is Type III Partial.

3.9 Optimization studies

Optimization was carried out to maximize material strength with the selected ranges of parameters (ST and HR). The best desirability of 0.985 out of four runs was selected for MH and RD, as shown in Fig. 14. Table 10 shows that the constraints measured applied for optimization.

4 Conclusion

This research successfully fabricated a novel $\text{Ni}_{14.29}\text{Al}_{14.29}\text{Ti}_{14.29}\text{Mn}_{14.29}\text{Co}_{14.29}\text{Fe}_{14.29}\text{Cr}_{14.29}$ High Entropy Alloy via a spark plasma sintering route. To improve the mechanical properties of this alloy, the process parameters (ST and HR) were optimized, and a predicting model was developed, with a minimum experimental run of 9 using RSM. The influence of each parameter on microhardness and relative density was observed, and the result indicates that temperature has more influence on its mechanical properties. At an ST of 850 °C and HR of 100 °C/min, maximum hardness (136.3 HV) and 99% densification (99.61) were attained. The results obtained from the Model; F -value, P -value, R^2 , Predicted R^2 , and Adeq Precision established the significance of the model developed. Therefore, comparing the experimental and the predicted values, the accuracy of the model developed was established.

Table 9 ANOVA table

Source	Sum of squares	df	Mean square	F -value	p -value	
Microhardness (HV)						
Model	74.05	2	37.02	278.07	<0.0001	Significant
A-Temperature (T)	69.22	1	69.22	519.90	<0.0001	
B-Heating Rate (HR)	4.82	1	4.82	36.23	<0.0009	
Residual	0.7989	6	0.1331			
Cor Total	74.85	8				
Relative density						
Model	9.94	2	4.97	166.84	<0.0001	Significant
A-Temperature (T)	9.39	1	9.39	315.35	<0.0001	
B-Heating Rate (HR)	0.5458	1	0.5458	18.33	<0.0052	
Residual	0.1787	6	0.0298			
Cor Total	10.12	8				

Fig. 14 Optimization result for MH and RD

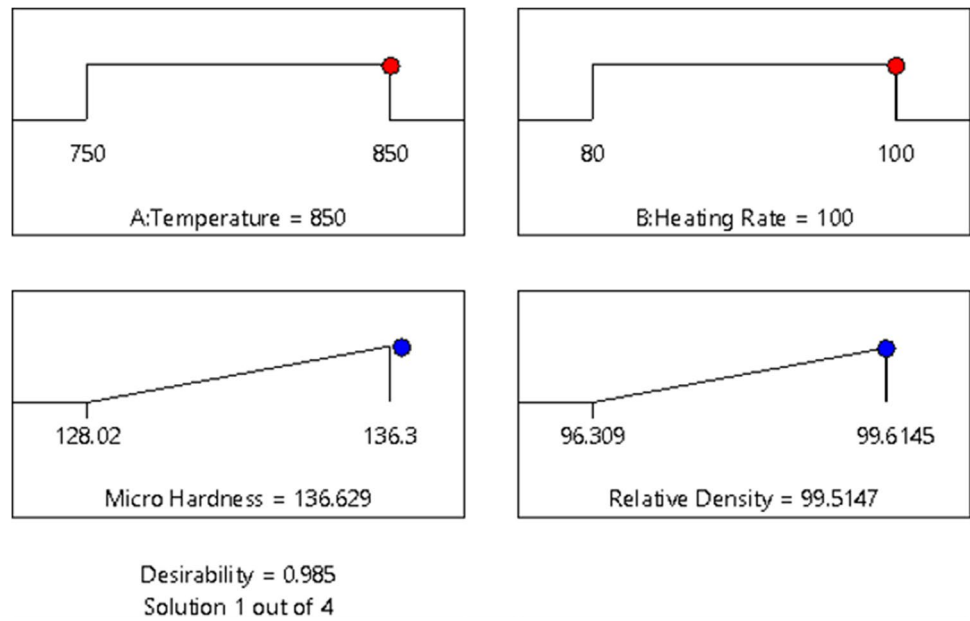


Table 10 Constraints measure for optimization

Name	Goal	Lower limit	Upper limit	Lower weight	Upper weight	Importance
A: T	Is in range	750	850	1	1	3
B: HR	Is in range	80	100	1	1	3
MH	Maximize	128.02	136.3	1	1	3
RD	Maximize	96.309	99.6145	1	1	3

Author contribution All authors involved contributed immensely to this research.

Funding Open access funding provided by University of Johannesburg. There is no special grant for this research. However, necessary support was given by the Department of Metallurgical Engineering of University of Johannesburg, Johannesburg, South Africa.

Data availability The data used in this research are not available publicly. However, it can be obtained from the authors once a justifiable request is made.

Declarations

Conflict of interest The authors declare no competing interests.

Open Access This article is licensed under a Creative Commons Attribution 4.0 International License, which permits use, sharing, adaptation, distribution and reproduction in any medium or format, as long as you give appropriate credit to the original author(s) and the source, provide a link to the Creative Commons licence, and indicate if changes were made. The images or other third party material in this article are included in the article's Creative Commons licence, unless indicated otherwise in a credit line to the material. If material is not included in the article's Creative Commons licence and your intended use is not permitted by statutory regulation or exceeds the permitted use, you will need to obtain permission directly from the copyright holder. To view a copy of this licence, visit <http://creativecommons.org/licenses/by/4.0/>.

References

- Ogunbiyi OF, Jamiru T, Sadiku ER, Adesina OT, Salifu SA, Beneke LW (2019) Effect of nickel powder particle size on the microstructure and thermophysical properties of spark plasma sintered NiCrCoAlTiW-Ta superalloy. In: Conf. South African Adv. Mater. Initiat. <https://doi.org/10.1088/1757-899X/655/1/012031>
- Kim SH, Shin GH, Kim BK, Kim KT, Yang DY, Aranas C, Choi JP, Yu JH (2017) Thermo-mechanical improvement of Inconel 718 using ex situ boron nitride-reinforced composites processed by laser powder bed fusion. Sci Rep 7:1–14. <https://doi.org/10.1038/s41598-017-14713-1>
- Jia Q, Gu D (2014) Selective laser melting additive manufacturing of TiC/Inconel 718 bulk-form nanocomposites: densification, microstructure, and performance. J Mater Res 29:1960–1969. <https://doi.org/10.1557/jmr.2014.130>
- Trojanová Z, Drozd Z, Lukáč P, Minárik P, Németh G, Seetharaman S, Džugan J, Gupta M(2020) Magnesium reinforced with Inconel 718 particles. Prepared ex situ—microstructure and properties, Materials (Basel) 13. <https://doi.org/10.3390/ma13030798>
- Wang Y, Shi J, Wang Y (2015) Reinforcing inconel 718 superalloy by nano-TiC particles in selective laser melting, ASME 2015 Int. Manuf Sci Eng Conf MSEC 2015(2):1–8. <https://doi.org/10.1115/MSEC20159365>
- Babalola BJ, Shongwe MB, Jeje SO, Rominiyi AL, Ayodele OO, Olubambi PA (2019) Influence of spark plasma sintering temperature on the densification and micro-hardness behaviour

- of Ni-Cr-Al alloy. IOP Conf Ser Mater Sci Eng 655:4195–4206. <https://doi.org/10.1088/1757-899X/655/1/012032>
7. Ebhota WS, Jen T-C (2018) Intermetallics formation their effect on mechanical properties of Al-Si-X Alloys. *Intermetallic Compounds - Formation and Applications*. <https://doi.org/10.5772/intechopen.73188>
 8. Habanyama A, Comrie CM (2018) Inter-diffusion of nickel and palladium germanium. *Intermetallic Compounds - Formation and Applications*. <https://doi.org/10.5772/intechopen.73190>
 9. Ishaq M, Basariya R, Mukhopadhyay K (2018) Structural and mechanical behaviour of Al-Fe intermetallics. *Intermetallic Compounds - Formation and Applications*. <https://doi.org/10.5772/intechopen.73944>
 10. Pope D (1996) Mechanical properties of intermetallic compounds, 4, Re, Elsevier B.V. <https://doi.org/10.1016/B978-0-444-89875-3.50029-6>
 11. Czeppe T, Wierzbinski S (2000) Structure and mechanical properties of NiAl and Ni₃ Al-based alloys. *Int J Mech Sci* 42. [https://doi.org/10.1016/S0020-7403\(99\)00087-9](https://doi.org/10.1016/S0020-7403(99)00087-9)
 12. Darolia R (2000) NiAl alloys for high temperature structural applications. *J Mater Sci* 10. <https://doi.org/10.1520/MPC20200183>
 13. Rogal Ł, Szklarz Z, Bobrowski P, Kalita D, Garzeł G, Tarasek A, Kot M, Szezynger M (2019) Microstructure and mechanical properties of Al–Co–Cr–Fe–Ni base high entropy alloys obtained using powder metallurgy. *Met Mater Int* 25:930–945. <https://doi.org/10.1007/s12540-018-00236-5>
 14. Yin X, Xu S (2018) Properties and preparation of high entropy alloys. *Matec Web Conf* 142:1–5. <https://doi.org/10.1051/matec/conf/201714203003>
 15. Tsai MH (2014) (Review) Physical properties of high entropy alloys. *Entropy* 15:5338–5345. <https://doi.org/10.3390/e15125338>
 16. Zhang Y, Beijing T, Zuo TT, Beijing T, Liaw P (2013) High-entropy alloys with high saturation magnetization, electrical resistivity, and malleability. *Sci Rep* 3:1455. <https://doi.org/10.1038/srep01455>
 17. Rajan RN, Rajendran S, Nagar AA (2014) High entropy alloys and corrosion resistance Section B-Review high entropy alloys and corrosion resistance – a bird ’ s eye view high entropy alloys and corrosion resistance – a bird ’ s eye view. *Eur Chem Bull* 3:1031–1035. <https://www.researchgate.net/publication/282913403.High>. Accessed 21 Dec 2022
 18. Qiu Y, Gibson MA, Fraser HL, Birbilis N, Gibson MA, Fraser HL, Corrosion NB, Qiu Y, Gibson MA, Fraser HL, Birbilis N (2016) Corrosion characteristics of high entropy alloys corrosion characteristics of high entropy alloys. *Mater Sci Technol* 0836. <https://doi.org/10.1179/1743284715Y.0000000026>
 19. Shi Y, Yang B, Liaw PK (2017) Corrosion-resistant high-entropy alloys : a review. *Metals (Basel)* 43:1–18. <https://doi.org/10.3390/met7020043>
 20. Miracle DB, Miller JD, Senkov ON, Woodward C, Uchic MD, Tiley J (2014) Exploration and development of high entropy alloys for structural applications. *Entropy* 16:494–525. <https://doi.org/10.3390/e16010494>
 21. Miracle DB, (2015) Critical assessment 14 : high entropy alloys and their development as structural materials. *Mater Sci Technol* 31. <https://doi.org/10.1179/1743284714Y.0000000749>
 22. Zhang Y, Ting T, Tang Z, Gao MC, Dahmen KA, Liaw PK, Ping Z (2014) Microstructures and properties of high-entropy alloys. *Prog Mater Sci* 61:1–93. <https://doi.org/10.1016/j.pmatsci.2013.10.001>
 23. Gludovatz B, Hohenwarter A, Catoor D, Chang EH, George EP, Ritchie RO (2014) A fracture-resistant high-entropy alloy for cryogenic applications. *J Sci* 345:1153–1158. <https://doi.org/10.1126/science.1254581>
 24. Diao HY, Feng R, Dahmen KA, Liaw PK (2017) Fundamental deformation behavior in high-entropy alloys : an overview. *Curr Opin Solid State Mater Sci*. <https://doi.org/10.1016/j.cossms.2017.08.003>
 25. Li W, Liaw PK, Gao Y (2018) Fracture resistance of high entropy alloys : a review. *Intermetallics* 99:69–83. <https://doi.org/10.1016/j.intermet.2018.05.013>
 26. Hitchcock D, Livingston R, Liebenberg D (2015) Improved understanding of the spark plasma sintering process. *J Appl Phys* 117:6–11. <https://doi.org/10.1063/1.4919814>
 27. Fayomi J, Popoola AP, Popoola O, Aigbodon V, Agboola O, The spark plasma sintering of the optimized parametric process for the magnesium alloy reinforced hybrid nano - ceramics. *Int J Adv Manuf Technol*. <https://doi.org/10.1007/s00170-022-10617-1>
 28. Liu H, Liu L, Xin C (2021) Effect of alloying elements on the structure and mechanical properties of NbMoTaW_X (X = Cr , V , Ti , Zr , and Hf) refractory high- entropy alloys Effect of alloying elements on the structure and mechanical properties of NbMoTaW_X (X = Cr , V , Ti , Zr. *J Appl Phys* 025044. <https://doi.org/10.1063/5.0038405>
 29. Li C, Li JC, Zhao M, Jiang Q (2009) Effect of alloying elements on microstructure and properties of multiprincipal elements high-entropy alloys. *J Alloys Compd* 475:752–757. <https://doi.org/10.1016/j.jallcom.2008.07.124>
 30. Olorundaisi E, Jamiru T, Adegbola TA, Ogunbiyi OF (2019) Modeling and optimization of operating parameters using RSM for mechanical behaviour of dual phase steels. *Mater Res Express*. 6:105628. <https://doi.org/10.1088/2053-1591/ab430e>
 31. Olorundaisi E, Jamiru T, Adegbola TA (2021) Response surface modelling and optimization of temperature and holding time on dual phase steel, In: *Materials Today: Proceedings*. Elsevier Ltd, 1164–1169. <https://doi.org/10.1016/j.matpr.2020.07.408>
 32. Seidenfeld T (1992) R.A. Fisher on the design of experiments and statistical estimation. In: Seidenfeld T (ed) *The Founders of Evolutionary Genetics Boston Studies in the Philosophy of Science*. Springer, Dordrecht, pp 23–24. https://doi.org/10.1007/978-94-011-2856-8_2
 33. Ogunbiyi O, Jamiru T, Sadiku R, Adesina O, LoluOlajide J, Beneke L (2020) Optimization of spark plasma sintering parameters of inconel LC alloy using response surface methodology (RSM). *Int J Light Mater Manuf* 3:177–188. <https://doi.org/10.1016/j.ijlmm.2019.10.002>
 34. Das A, Sarkar S, Karanjai M, Sutradhar G (2018) RSM based study on the influence of sintering temperature on MRR for titanium powder metallurgy products using Box-Behnken design. *Mater Today Proc* 5:6509–6517. <https://doi.org/10.1016/j.matpr.2018.01.137>
 35. Yang K, El-Haik B (2003) *Design for six sigma A roadmap for product development*. McGraw-Hill, New York. <https://doi.org/10.1036/0071435999>
 36. Myers RH, Montgomery DC, Anderson-Cook CM (2009) *Response surface methodology, 3rd edn*. John Wiley & Sons Inc, New Jersey
 37. Muthuraj R, Misra M, Mohanty AK (2015) Studies on mechanical, thermal, and morphological characteristics of biocomposites from biodegradable polymer blends and natural fibers. In: *Biocomposites Des. Mech. Perform., Fourteenth*, Elsevier Ltd., pp 93–140. <https://doi.org/10.1016/B978-1-78242-373-7.00014-7>
 38. Wang M, Cui H, Zhao Y, Wang C, Wei N, Zhao Y, Zhang X, Song Q (2019) A simple strategy for fabrication of an FCC-based complex concentrated alloy coating with hierarchical nanoprecipitates and enhanced mechanical properties. *Mater Des* 180:107893. <https://doi.org/10.1016/j.matdes.2019.107893>
 39. Aguilar C, Martinez C, Tello K, Palma S, Delonca A, San Martín F, Alfonso I (2020) Thermodynamic analysis of the formation of FCC and BCC solid solutions of ti-based ternary alloys by

- mechanical alloying, *Metals* (Basel). 10.: <https://doi.org/10.3390/met10040510>.
40. Hosford FW (2010) *Mechanical behavior of materials*, 2nd edn. Cambridge University Press, New York
41. Meyers MA, Chawla KK (2009) *Mechanical behavior of materials*. Cambridge University Press. <https://books.google.co.za/books?id=LXcjEAZ9tX4C>
42. Ashby MF, Jones DRH (2013) *Metal structures* (2nd edn). Elsevier Inc. <https://doi.org/10.1016/b978-0-08-096668-7.00002-4>
43. Hull D, Bacon DJ (2011) Dislocations in face-centered cubic metals. In: *Introd. to Dislocations*, pp 85–107. <https://doi.org/10.1016/b978-0-08-096672-4.00005-0>
44. Ogunbiyi OF, Jamiru T, Sadiku ER, Beneke L, Adesina OT, Adegbola TA (2019) Influence of sintering temperature on microstructural evolution of spark plasma sintered Inconel738LC. *Procedia Manuf* 35:1152–1157. <https://doi.org/10.1016/j.promfg.2019.06.070>
45. Adesina OT, Jamiru T, Sadiku ER, Durowoju MO, Ogunbiyi OF (2019) Mechanical performance of GNP/PLA nanocomposite under varied SPS process parameters. In: 4th Int. Conf. Des. Manuf. Eng., pp 0–5. <https://doi.org/10.1088/1757-899X/627/1/012017>
46. Adesina OT, Sadiku ER, Jamiru T, Ogunbiyi OF, Beneke LW, Adegbola AT (2019) Optimization of SPS processing parameters on the density and hardness properties of graphene reinforced polylactic acid nanocomposite. *Int J Adv Manuf Technol* 102:4047–4058. <https://doi.org/10.1007/s00170-019-03530-7>
47. Oketola A, Jamiru T, Adegbola AT, Ogunbiyi O, Rominiyi AL, Salifu S (2022) Spark plasma sintering of ZrO₂ reinforced Ni-Cr alloy: microstructure and mechanical behavior. *J Compos Mater* 56:3553–3562. <https://doi.org/10.1177/00219983221113009>
48. Khuri AI, Mukhopadhyay S (2010) Response surface methodology, *Wiley Interdiscip. Rev. Comput Stat* 2:128–149. <https://doi.org/10.1002/wics.73>
49. Saldaña-Robles A, Guerra-Sánchez R, Maldonado-Rubio MI, Peralta-Hernández JM (2014) Optimization of the operating parameters using RSM for the Fenton oxidation process and adsorption on vegetal carbon of MO solutions. *J Ind Eng Chem* 20:848–857. <https://doi.org/10.1016/j.jiec.2013.06.015>
50. Montgomery D (2002) *Design and analysis of experiments. Quality and Reliability Engineering International*, 5th edn. John Wiley and Sons, New York City, pp 163–163. <https://doi.org/10.1002/qre.458>
51. Shuster JJ (2007) Design and analysis of experiments. *Methods Mol Biol* 404:235–259. <https://doi.org/10.2307/2985452>
52. Hou TH, Su CH, Liu WL (2007) Parameters optimization of a nano-particle wet milling process using the Taguchi method, response surface method and genetic algorithm. *Powder Technol* 173:153–162. <https://doi.org/10.1016/j.powtec.2006.11.019>
53. Olorundaisi E, Ikele O, Jamiru T, Adesola AT, Fayomi J, Akhiwu B (2021) Optimization and microstructural evaluation of processing parameters on the density and surface hardness of dual phase steel. *Sci J Res Rev* 3:1–14. <https://doi.org/10.33552/sjrr.2021.03.000553>

Publisher's note Springer Nature remains neutral with regard to jurisdictional claims in published maps and institutional affiliations.